Applied Thermal Engineering 242 (2024) 122542

Contents lists available at ScienceDirect

Applied Thermal Engineering

journal homepage: www.elsevier.com/locate/ate

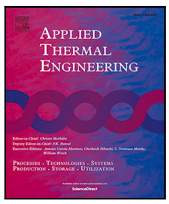

Research Paper

Experimental investigation of two-phase flow in Chevron-type compact plate heat exchangers: A Study on pressure drops and flow regimes visualization

Stefano Passoni [a], Andrea Ferrario [a], Marco E. Ricotti [b], Riccardo Mereu [a,*]

[a] Politecnico di Milano, Department of Energy, via Lambruschini 4a, Milano, 20156, Italy
[b] Politecnico di Milano, Department of Energy, Nuclear Engineering Division, via La Masa 34, Milano, 20156, Italy

ARTICLE INFO

Keywords:
Multiphase flow
Compact plate heat exchanger
Two-phase pressure drop
Flow regime visualization
Flow regime transition

ABSTRACT

Compact plate heat exchangers are a very promising technology and lately they are being considered for potential use as steam generators in Small Modular Reactors. However, there is a lack of scientific literature on their operation with two-phase flows, especially with non-refrigerant fluids. In this study, we conducted experiments to visualize and measure the pressure drop of a two-phase flow in a Chevron-type Plate Heat Exchanger. An air–water mixture was used in adiabatic conditions as the operating fluid in upward-flow configuration. Visualization was achieved through high-framerate videos. This study covers a wide range of operating conditions, surpassing those documented in existing literature by specifically analyzing also the region of very low mass flux for both phases. The tested conditions ranged from 6 to 365 kg/m^{2}s of water and from 0.02 to 5 kg/m^{2}s of air. Single-phase pressure drops were measured to establish a correlation for the Darcy friction factor. Instead, measurements of the pressure drop in two-phase conditions were processed and presented using a non-dimensional form referred to as the two-phase multiplier. The adoption of a void-fraction model played a crucial role in accurately extrapolating the frictional component of the pressure drop from the measurements, resulting in less scattered data on the Lockhart–Martinelli plot. In addition, the observed flow structures were categorized into distinct regimes (fine-coarse bubbly, Taylor-like bubbly, heterogeneous, partial film, and film flow) based on visual observation and were represented on a flow map. Finally, these data were used to develop new criteria for predicting flow pattern transitions.

1. Introduction

Plate Heat Exchangers (PHEs) are a type of industrial heat exchanger that consists of stacked corrugated plates, which can be gasketed or sealed through brazing or welding. These components offer several advantages like a very high performance to volume ratio, making them superior to other heat exchanger types like shell and tube designs. The corrugated profile of the plates promotes turbulence on both the hot and cold sides, thereby enhancing heat transfer efficiency. For this reason, compact PHEs are lately being considered as steam generators in different kind of application such as Small Modular Nuclear Reactors (SMRs) where their small volume is an essential characteristic. For example, Kang et al. [1] recently conducted a numerical investigation to assess the feasibility of adopting a steam generator with corrugated plates in SMRs. A detailed analysis of multiphase fluid dynamics enables the development of accurate correlations and models for predicting pressure drops, heat transfer coefficients, and flow regime transitions. These correlations and models can guide the design process, allowing engineers to optimize the geometries, plate configurations, and operational parameters of compact plate heat exchangers for specific applications. The investigation of single-phase flow behavior in Plate Heat Exchangers (PHEs) has been extensively studied. Ayub's review [2] provides a comprehensive summary of correlations for single-phase flows in PHEs. Additionally, handbooks and papers specifically intended for the design of PHEs under single-phase flow conditions are also present in literature. In the VDI Heat Atlas [3] Martin presented correlations for evaluating pressure drop and heat transfer in PHEs of different geometries. Thulukkanam [4] described in detail the many different configurations of PHEs and the approach to be used in the design phase. Kakac et al. [5] dedicated a chapter of their book to PHEs, presenting correlations for evaluating thermo-hydraulic performances. Wang et al. [6] published a comprehensive book on PHEs covering industrial applications, manufacturing, design, and operational aspects of these components. In their book Klemes et al. [7] analyzed the applications of compact heat exchangers for

* Corresponding author.
E-mail addresses: stefano.passoni@polimi.it (S. Passoni), andrea1.ferrario@polimi.it (A. Ferrario), marco.ricotti@polimi.it (M.E. Ricotti), riccardo.mereu@polimi.it (R. Mereu).

https://doi.org/10.1016/j.applthermaleng.2024.122542
Received 30 August 2023; Received in revised form 19 January 2024; Accepted 23 January 2024
Available online 24 January 2024

Nomenclature

Latin Letters

A_f [m^2]	Frontal Area
A_{fl} [m^2]	Float projected area
A_r [m^2]	Rotameter section
B_p [m]	Plate Width
b_p [m]	Corrugation depth
C_0 [–]	Distribution parameter
C_d [–]	Drag Coefficient
D_h [m]	Hydraulic Diameter
d_{max} [m]	Maximum bubble/drop diameter
e_i [$i_{U.O.M.}$]	Uncertainty of quantity "i"
f_D [–]	Darcy friction factor
G [kg/m^2 s]	Mass Flux
g [m/s^2]	Gravitational Constant
J [m/s]	Mixture Velocity
L_p [m]	Corrugated section length
M [m]	Bubble maximum diameter Multiplier
M_{fl} [kg]	Float Mass
P [Pa]	Absolute Pressure
Q [m^3/s]	Volumetric Flow Rate
R^* [J/kgK]	Specific Gas Constant (Gas constant divided by molar mass)
Re [–]	Reynolds number
s [–]	Slip Ratio
T [K]	Absolute Temperature
U_{gj} [m/s]	Drift Velocity
U_G [m/s]	Gas Actual Velocity
v [m/s]	Velocity
$v_{s,G}$ [m/s]	Gas Superficial Velocity
$v_{s,L}$ [m/s]	Liquid Superficial Velocity
X [–]	Lockhart–Martinelli Parameter
x [–]	Mass Quality
x_v [–]	Volume Quality

Greek Letters

α [–]	Void Fraction
χ [–]	Wave number
ϵ [m^2/s^3]	Turbulent kinetic energy dissipation rate
λ [m]	Corrugation Wavelength
μ [kg/ms]	Dinamic Viscosity
Φ [–]	Enlargement factor
Φ_{TP} [–]	Two-Phase Multiplier
ρ [kg/m^3]	Density
σ [N/m]	Surface Tension
θ [°]	Inclination of the channel
φ [°]	Corrugation Angle

Thermo-Fluid Dynamic Properties Subscripts

$2ph$	Two-Phase
cal	Calibration
f	Fluid
G	Gas phase
g	Gas flowing alone
gj	Gas Drift (velocity)
in	Inlet
L	Liquid phase
l	Liquid flowing alone
low	At transmitter low end
m	Bulk/mixture (density)
$meas$	Measured
out	Outlet
pl	Plate/Channel
$read$	Reading
rot	Rotameter
s	Superficial/apparent (velocity)

recovering waste heat, dedicating a significant portion of their specific applications and provide correlations for heat transfer coefficient and friction factor that are limited and lack of generality. This is mainly due to the fact that complexity due to the two-phase flow is also emphasized by the complex geometry of the plates. The recent reviews of Ayub et al. [8], Amalfi et al. [9] and Eldeeb et al. [10] all agree that, despite the many proposed correlations, a common issue is the lack of generality. Both Amalfi et al. [9] and Ayub et al. [8] tried to address this problem by introducing new correlations. Moreover, the use of specific fluids like refrigerants for studying phase-change phenomena also limits the range of mass fluxes tested during the experimental works.

Unlikely what has been done for two-phase flows in more common components like pipes, two-phase fluid dynamics in PHE has yet to be studied in deep. Several authors worked on the topic, mostly from early 2000s and on. The different works mainly differentiate one from another by the geometry adopted, whether the testing was carried out in adiabatic condition or not, the flow direction and the range of the operating conditions. Among the authors that operated their facility with air and water we find Tribbe and Müller–Steinhagen [11,12], Vlasogiannis et al. [13], Grabenstein et al. [14] and Buscher [15,16]. They all focused on single and two-phase pressure drop measurement and modeling while not everyone visualized the flow during the operation of the component. Fig. 1 illustrates the operating conditions explored in the above-mentioned experimental studies, as well as the domain related to the present work. The representation is based on liquid and gas superficial velocities. It is evident from the figure that there is an overlap among the studies but only at intermediate values of both phases velocities. This indicates a convergence in the exploration of operating conditions within this range across multiple studies. In addition to this, our study wants also to cover the region of low gas and liquid velocities ($0.006\,[m/s] < v_{s,G} < 0.03\,[m/s]$, $0.007\,[m/s] < v_{s,L} < 0.05\,[m/s]$). This area of investigation is still unexplored, yet it holds significant importance, for instances in scenarios where the total flow rate of a plate heat exchanger is distributed among a great number of channels leading to a notably low specific mass flux.

When measuring the pressure drop of a two-phase flow it is important to distinguish between the frictional part of the pressure drop, the gravitational and the accelerative one. In PHE operated with air and water mixture, since the assumption of constant section area and incompressible fluid holds true, the accelerative component turns out to be very low and can always be neglected [16]. To correctly remove the gravitational component from the measurements one should have a really accurate void fraction model but, to the knowledge of the authors, it has yet to be provided in literature. Therefore a common approach is to make the unphysical hypothesis of considering the flow as homogeneous. Buscher in [16] proposed the usage of a constant "hydrostatic correction factor" by comparing measurements in upward and downward configurations to the horizontal one in which the gravitational components tends to zero. In this work, the data provided by Asano in [17,18] will be used to propose a drift flux model to best estimate the void fraction in chevron-type corrugated channels. In that

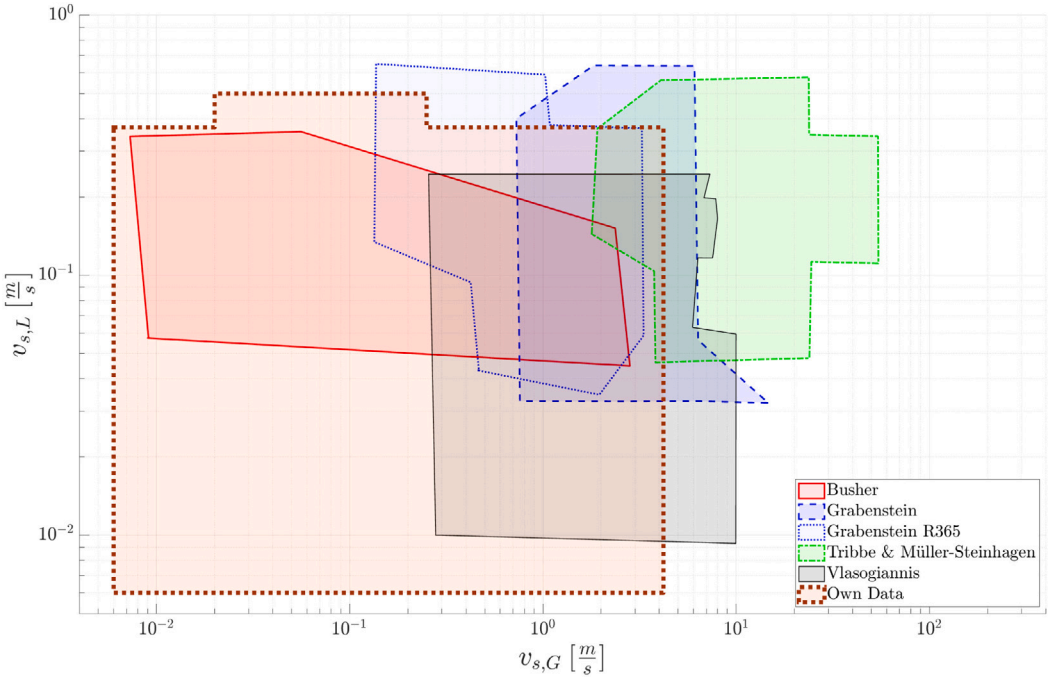

Fig. 1. Visual representation of the operating conditions explored in various experimental studies on the topic.

work, the author measured the void fraction of an air and water mixture in a PHE by means of intensity analysis on images obtained by neutron radiography

This study seeks to thoroughly investigate the measurement of pressure drops in both single-phase and two-phase flows, along with the visualization and categorization of flow patterns within a Chevron-type corrugated channel using a mixture of air and water as the working fluid. Unlike existing literature, this manuscript aims to encompass a broader spectrum of operating conditions to provide a complete reference for all the phenomena that are present at various flow rates. By exploring a broad range of operating parameters including very low mass fluxes for both phases, a reliable model of the void fraction in the channel revealed to be crucial to estimate the gravitational component of pressure drops. For this purpose, a drift-flux model was employed and proved to be effective in modeling such quantity. In the end, this study aims at providing valuable insights and correlations that can be applied across various applications and conditions involving Chevron-type corrugated channels.

After the introduction, in Section 2 the experimental setup is described and discussed in terms of plant layout and instrumentation as well as data reduction and uncertainty analysis. Section 3 reports the main findings of the work. Flow patterns are visualized and classified, single-phase pressure drops are analyzed in the form of Darcy's friction factor and two-phase pressure drops are illustrated on a Lockhart–Martinelli plot highlighting the importance of the model employed to predict the void fraction. The obtained results were applied for developing criteria for flow patterns prediction. Lastly, in Section 4, the conclusion of the present work are drawn.

2. Materials and methods

2.1. Experimental layout

The experimental tests for flow visualization and pressure drop measurement were conducted using the adiabatic loop depicted in Fig. 2. The setup consists of a closed-loop water circuit connected to an open-loop compressed air circuit. The water circuit is supplied by a centrifugal pump (CALPEDA NMM/AE) with a flow rate range of 1 to 4.2 m^3/h and a head range of 16.3 to 22 m. Flow rates were measured using three rotameters covering different ranges and controlled using needle valves at their respective outlets. Compressed air is supplied through a centralized line and its pressure is reduced using a pressure-regulation valve to achieve the desired target pressure. The air flow rate is also measured using three rotameters, and their readings are corrected to account for pressure and temperature deviations from calibration conditions. Detailed characteristics of the flow meters are provided in Table 1. Additionally, a bypass line is included in the circuit to facilitate startup operations. To ensure proper mixing of the two fluids before entering the visualization facility, a special mixing section was designed. Both the air and water lines are divided into two branches and fed into two distributors, each dividing the flow into four smaller-diameter lines where mixing occurs through T-junctions. Regulation valves are employed to ensure balanced flow rates between the feeding tubes. Subsequently, the two-phase mixture enters a plenum containing a perforated plate, which homogenizes the flow before it enters the corrugated channel. At the outlet of the channel, the mixture flows into a collector and is then directed back to the feeding tank, where air is spontaneously vented.

The facility was operated in the upward configuration, with water mass flux ranging from 6 to 365 kg/m^2 s and air mass flux ranging from 0.02 to 5 kg/m^2 s. The operating temperature of the air was maintained between 18 °C and 21.5 °C, while the water temperature varied between 23 °C and 26 °C, primarily due to the heating effect from the pump. Pressure taps were positioned on the inlet and outlet plenum, as close as possible to the corrugated channel. Differential pressure was measured using transmitters, and their signals were sampled at a frequency of 4 Hz for a duration of 30 s via a data acquisition system (Agilent 34970 A). The acquired data were later processed using MATLAB® to extract meaningful statistics. Specific characteristics of the pressure transmitters are provided in Table 2. To measure the operating gauge pressure of the plate, a manometer was installed downstream from the high-pressure ports. Given its considerable variation, ranging from 3 to 30 kPa, clamps were applied to the lower part of the visualization window to mitigate plate deformation and prevent the loss of contact points. Plate deformation is a critical issue in this type of application and to ensure accurate results a preliminary analysis was carried out to identify a range of operating conditions

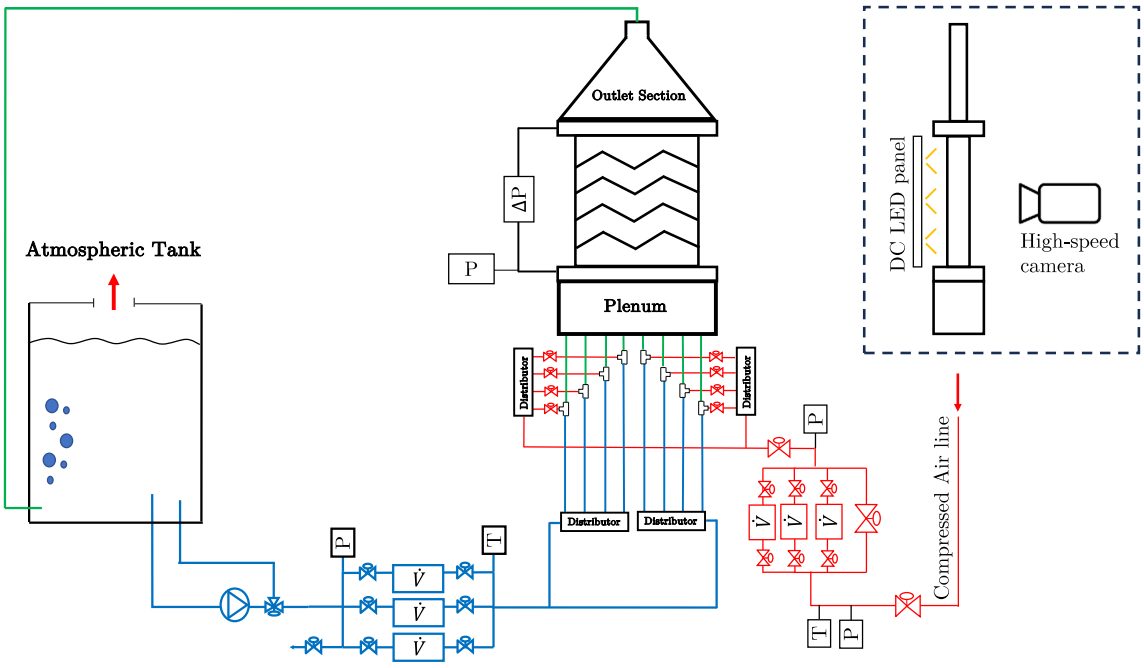

Fig. 2. Scheme of the experimental loop of the present work and detail of the setup used for flow visualization.

Table 1
Characteristics of flowmeters.

ASAMETRO	P13–2500	P13–2600	P13–2900	E5–2600	E5–2600	E5-2600
Fluid	Water	Water	Water	Air	Air	Air
Range	10–100 L/h	40–400 L/h	250–2500 L/h	4–190 nL/h	100–800 nL/h	400–4000 nL/h
Uncertainty	±3% full scale	±3% full scale	±3% full scale	±2% full scale	±2% full scale	±2% full scale
Tcal	20 °C	20 °C	20 °C	20 °C	20 °C	20 °C
Pcal	–	–	–	101.33 kPa	101.33 kPa	101.33 kPa

Table 2
Characteristics of pressure transmitters.

Model	Klay DP-4000	Klay DP-4000	Klay DP-4000	SETRA 267 MR 7
Fluid	Water/Air	Water/Air	Water/Air	Air
Range	0–60 mbar	0–400 mbar	0–2000 mbar	0–250/0–1000 Pa
Measure type	Differential	Differential	Differential	Differential
Accuracy	0.075%	0.075%	0.075%	1%
Output	4-20 mA	4-20 mA	4-20 mA	0–5 V

where no deformation occurs. The study was conducted in single phase, revealing an abrupt change in the friction factor curve's slope for mass fluxes above 610 $\frac{kg}{m^2\ s}$. which was associated with plate deformation. This phenomenon manifested at plate operating pressures exceeding 30 kPa. Consequently, this pressure was established as the upper limit for the explored range of measurements in both single and two-phase scenarios.

The experimental visualization section, as depicted in Fig. 3, comprised two transparent replica plates designed to simulate the behavior of a corrugated channel in a plate heat exchanger while enabling flow visualization. To create the transparent plates, a custom silicon mold was made using the original steel plates illustrated in Fig. 4. Resin was then poured into the mold, resulting in nearly 3 cm thick transparent plates. These plates were securely enclosed within a bolted steel frame to ensure perfect contact during the experiments. The chevron pattern on the plates featured corrugation angles of 63° and grooves 2.5 mm deep. For further geometrical details the reader may refer to Table 3 while a visual representation of these parameters is available in Fig. 5. The frontal area of the corrugated channel was approximated with the product of channel width and the mean channel height that is one time the corrugation depth, employing the following formula:

$$A_f = b_P \cdot B_p \tag{1}$$

The error due to this approximation is less than 3.4% as described in Appendix A. The enlargement factor is the ratio between the effective plate surface and the area of a flat plate with same length and width and, in the present work, it was computed by numerical integration of the sinusoidal function resulting in

$$\Phi = \frac{1}{6}\left(1 + \sqrt{1+\chi^2} + 4\sqrt{1+\frac{\chi^2}{2}}\right) \tag{2}$$

$$\text{with} \quad \chi = \frac{\pi b_p}{\lambda} \tag{3}$$

The hydraulic diameter can be calculated assuming the plate width is significantly larger than corrugation height by:

$$D_h = \frac{2b_p}{\Phi} \tag{4}$$

To visualize the flow patterns at the various operating conditions, the corrugated channel was back-lit with a flicker-free DC white LED panel, providing consistent illumination. High frame rate videos were recorded using a Phantom Miro C110 high framerate camera. To capture fast-flowing phenomena the camera's sampling rate was set at 1900 frames per second, enabling the capture of rapid flow changes and intricate flow patterns with high temporal resolution. The videos

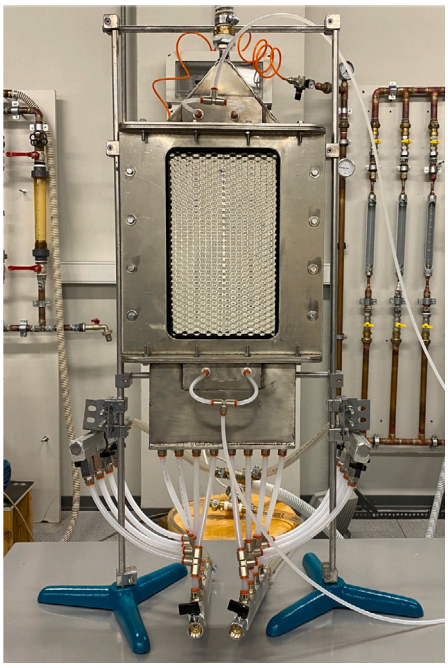

Fig. 3. Picture of the facility used for the experimental tests.

Fig. 4. Section of the original plate with the Chevron pattern adopted in the experiments.

Table 3
Geometrical parameters of present study's plates.

Corrugation Angle	φ	63°
Corrugation Depth	b_p	2.5 mm
Corrugation Wavelength	λ	9 mm
Plate Width	B_p	182 mm
Plate/Corrugation Length	L_p	320 mm
Enlargement Factor	Φ	1.1712
Frontal Area	A_f	455 mm^2
Hydraulic Diameter	D_h	4.3 mm

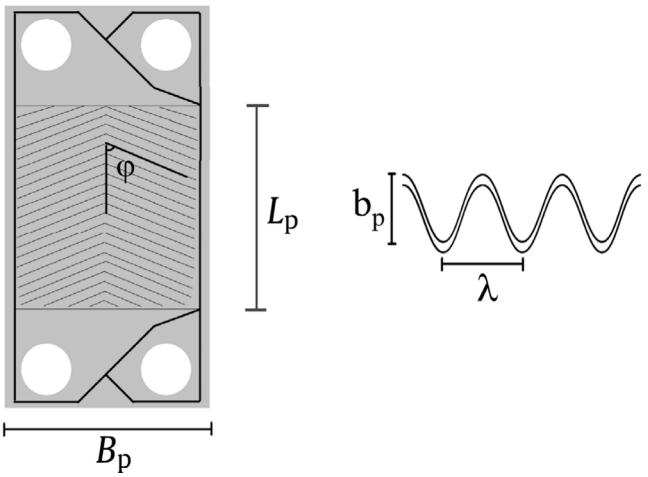

Fig. 5. Visual representation of the geometrical parameters of the plate and the corrugation profile.

were recorded at a resolution of 1280x480 pixels, ensuring clear and accurate visualization. The exposure time of the camera was carefully adjusted to 40 μs to provide correct brightness levels across the frame. The videos were captured using a NIKKOR AF-S Micro 60 mm lens. The lens was manually adjusted for focus and aperture settings to ensure precise control over the depth of field and sharpness of the images.

2.2. Data reduction methodology and uncertainty analysis

Prior to presenting the results, it is essential to address the methodology used to extract data from the measurements and post-process the experimental data.

As mentioned earlier in the preceding section, the gas flow rate reading was adjusted to accommodate deviations from the calibration conditions. Specifically, due to the operational characteristics of float-type flow rate measurement devices, it is necessary to consider variations in both pressure and temperature. To correct the flowmeter reading (Q_{read}), the following equation was employed. This expression was derived from a hydrodynamic force balance on the float and accounts for the dissimilar conditions between in the rotameters and the corrugated channel, assuming ideal gas behavior:

$$Q = \frac{\left(P_{rot} P_{cal}\right)^{0.5}}{P_{pl}} \left(\frac{T_{pl}}{T_{cal}}\right)^{0.5} Q_{read} \tag{5}$$

Here, P_{rot} represents the operating absolute pressure of the rotameter [Pa], measured using the upstream manometer. P_{cal} and T_{cal} refer to the calibration absolute pressure [Pa] and temperature [K], while P_{pl} and T_{pl} denote the absolute pressure $[Pa]$ and temperature $[K]$ of the mixture within the corrugated channel. It is important to note that the correction mentioned above is not required for the liquid flow rate, as its properties can be assumed constant within the range of varying operating temperature and pressure. A complete derivation of Eq. (5) can be found in Appendix B.

Single-phase friction factor was calculated following the Darcy's formulation as:

$$f_D = \frac{\Delta P}{\frac{1}{2}\rho v^2 \frac{L_p}{D_h}} = \frac{2\Delta P D_h A_f{}^2}{\rho Q^2 L_p} \tag{6}$$

where ΔP is the differential pressure measured between the pressure ports and Q the flow of either water or gas (corrected as Eq. (5) in this case).

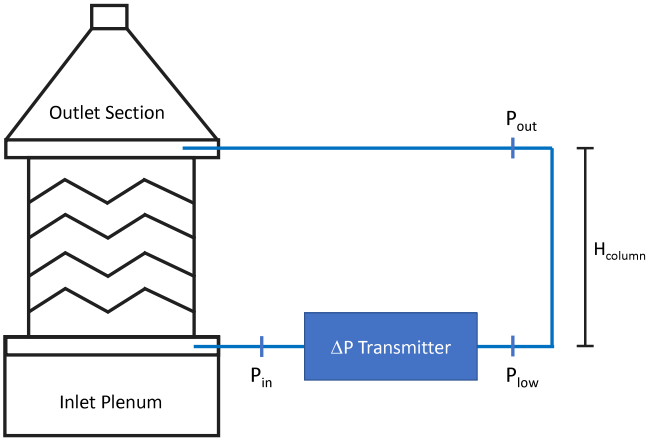

Fig. 6. Two-phase pressure drop measurements setup.

In two-phase flow, the total pressure gradient is the sum of three components: frictional, gravitational and accelerative pressure drop:

$$\left(\frac{dP}{dz}\right)_{total,2ph} = \left(\frac{dP}{dz}\right)_{fric,2ph} + \left(\frac{dP}{dz}\right)_{grav,2ph} + \left(\frac{dP}{dz}\right)_{acc,2ph} \tag{7}$$

where:

$$\left(\frac{dP}{dz}\right)_{grav,2ph} = -\rho_m \cdot g \cdot sin(\theta) \tag{8}$$

$$\left(\frac{dP}{dz}\right)_{acc,2ph} = -\frac{d\left(\frac{G^2}{\rho_m}\right)}{dz} \tag{9}$$

ρ_m represents the density of the two-phase mixture, θ denotes the clockwise angle from horizontal, and G the mass flux. The accelerative pressure drop refers to the pressure change associated with the density variation in the channel, which is generally considered negligible [16] in Plate Heat Exchangers (PHEs), especially when phase change is not present, as in the current study. Therefore, the global ΔP is the sum of frictional and gravitational components.

In Fig. 6 is reported the setup adopted for the pressure drops measurements. The pressure transmitter measures the pressure difference at its specific vertical location, resulting in a disparity between the measured pressure difference (ΔP) and the actual pressure difference between inlet and outlet. In the current setup, the tubes connecting the sensor to the pressure taps were consistently filled with water. As a result, the pressure at the lower-pressure side end of the sensor was higher than the pressure at the outlet of the corrugated channel because of the presence of the water column. Since there is no water flowing through the transmitter the pressure at channel outlet can be computed from transmitter low end by subtracting the hydrostatic head:

$$P_{out} = P_{low} - \rho_L\, g\, H_{column} \tag{10}$$

$$\Delta P_{meas} = P_{in} - P_{low} \tag{11}$$

Combining Eq. (10) with Eq. (11) the global ΔP can be computed from the measured ΔP:

$$\Delta P_{total,2ph} = P_{in} - P_{out} = P_{in} - P_{low} + \rho_L\, g\, H_{column} = \Delta P_{meas} + \rho_L\, g\, H_{column} \tag{12}$$

In order to analyze the frictional component a common approach consist in subtracting the gravitational one from the global pressure drops.

$$\Delta P_{fric,2ph} = \Delta P_{total,2ph} - \Delta P_{grav,2ph} \tag{13}$$

The integration of Eq. (8) leads to an equation for gravitational pressure drops, the density that should be adopted is a weighted average on void fraction and is obtained rigorously by a mono-dimensional momentum balance on the system.

$$\Delta P_{grav,2ph} = \rho_m\, g\, L_p \tag{14}$$

$$\rho_m = (1-\alpha)\,\rho_L + \alpha\,\rho_G \tag{15}$$

By substituting Eq. (14) and (15) into Eq. (13), it is possible to express the frictional pressure drops as a function of the measured pressure difference (ΔP) and void fraction.

$$\Delta P_{fric,2ph} = \Delta P_{meas} + \left(\rho_L - \rho_m\right)\, g\, L_p = \Delta P_{meas} + \alpha\,\left(\rho_L - \rho_G\right)\, g\, L_p \tag{16}$$

Particular attention must be paid to the computation of the mixture density. The typical approach in the literature [11,12,14–16] is to utilize the homogeneous flow model for calculating the void fraction, which is determined as the volumetric quality $\alpha_{hom} = x_v = \frac{Q_G}{Q_G+Q_L}$ and calculate mixture density as:

$$\rho_m = (1-x_v)\,\rho_L + x_v\rho_G \tag{17}$$

The validity of this model hinges on the assumption of no slip between the two phases. However, it is crucial to highlight that no void fraction model specifically developed for Plate Heat Exchangers (PHEs) currently exists. Utilizing existing models developed for pipes could introduce substantial errors due to the distinct geometry and resulting flow field in PHEs. Asano et al. [17,18] conducted visualizations of two-phase flow in a plate heat exchanger using neutron radiography. They computed void fraction distribution through intensity analysis on the acquired images. The data reported in their works were then processed using the drift-flux model formulated by Zuber and Findlay [19] to enhance the prediction of alpha. As part of their approach, they proposed to correlate the actual gas velocity ($U_G = v_{s,G}/\alpha$) with the mixture velocity ($J = v_{s,G} + v_{s,L}$) by adopting two parameters known as the distribution parameter (C_0) and the drift velocity (U_{gj}), as described by the following equation:

$$U_G = C_0 J + U_{gj} \tag{18}$$

The outcome of this model is a predictor of α expressed as:

$$\alpha = \frac{x_v}{\left(C_0 + \frac{U_{gj}}{J}\right)} \tag{19}$$

Zuber and Findlay [19] demonstrated that the fitting parameters exhibit a strong dependence on the flow patterns. In this study, the distribution parameter and drift velocity were treated as constants and calibrated using Asano's data [18]. As Asano suggested a different behavior for the separated flow regimes, two separate interpolations were proposed: one for low mixture velocities and another for high mixture velocities, with a threshold at 3 m/s. Fig. 7 illustrates the good agreement between the data obtained by Asano et al. using two different experimental setups. The linear interpolation (constant parameters) well fits the experiments with $C_0 = 1.4795$ and $U_{gj} = 0.2337$ for $J < 3$ m/s and $C_0 = 1.1653$ and $U_{gj} = 1.1229$ for $J > 3$ m/s. This interpolation is expected to hold true for own data since the operating fluids are the same (air/water) and the plates geometry is comparable (corrugation angle $\varphi = 60°$, $b_p = 1.4$ mm and $\lambda = 6.4$ mm).

In this study, the method proposed by Lockhart and Martinelli in [20] was employed to characterize two-phase pressure drops. This model expresses the two-phase pressure drops as a function of the pressure drops that the single phases would experience if they were flowing individually through the channel. Lockhart and Martinelli conducted their analysis in dimensionless form, introducing the Lockhart–Martinelli parameter X and the Two-phase multiplier Φ_{TP} to represent these pressure drops:

$$X = \sqrt{\frac{\left(\frac{dP}{dz}\right)_l}{\left(\frac{dP}{dz}\right)_g}} \tag{20}$$

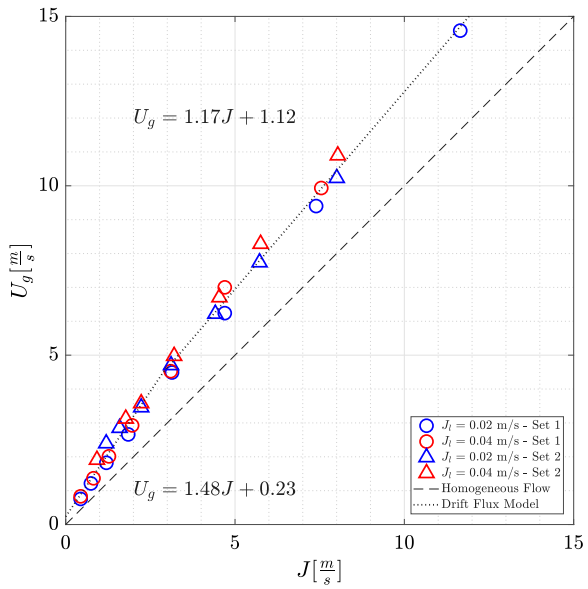

Fig. 7. Drift flux interpolation of experimental data from Asano et al. (Set 1 [17], Set 2 [18]).

$$\Phi_{TP} = \sqrt{\frac{\left(\frac{dP}{dz}\right)_{2ph}}{\left(\frac{dP}{dz}\right)_{l}}} \tag{21}$$

The Lockhart–Martinelli parameter X quantifies the relative significance of the pressure drop experienced by one phase compared to the other when they flow individually. On the other hand, the Two-phase multiplier Φ_{TP} indicates the increase in pressure drops attributed to the presence of the gaseous phase in addition to the single-phase liquid flow. Lockhart and Martinelli observed that these parameters exhibit a strong correlation when plotted on a chart. Chisholm [21] proposed an expression that effectively represents this correlation.

By utilizing the two-phase multiplier, one can easily calculate the two-phase pressure drops based on the pressure drops of the liquid flowing alone, employing the following equation:

$$\Delta P_{fric,2ph} = \Phi_{TP}^2 \cdot \Delta P_l \tag{22}$$

The liquid and gas frictional pressure drop of Eq. (20) could be derived from a model for single-phase friction factor or by directly correlating the experimental pressure drops to reach a higher accuracy. In the present work the latter method was employed.

2.3. Uncertainty analysis

The expanded uncertainties (u_{exp}) associated with the experimental data were determined following the standard procedure outlined in the JCGM 100:2008 guide [22]. For each data point acquired during the experiments, the expanded uncertainties were calculated individually and subsequently depicted as error bars on the corresponding plots. The sources of uncertainty considered in the analysis include the flow rate reading, the pressure drop measurement, and the analog manometer reading required for correcting the gas flow rate (P_{rot}) reading. The accuracy of the flowmeters and pressure transmitters used in the experiments was previously reported in Table 1 and Table 2, respectively. Additionally, the analog manometer had an accuracy of 10 kPa, representing the value of each tick on the reading scale.

In this study, the pressure drop results for single-phase operations are presented using the Reynolds number Re and Darcy friction factor f_D, while for two-phase operations, the Lockhart–Martinelli parameter X and Two-phase multiplier Φ_{TP} are utilized. The uncertainties associated with these parameters were calculated by combining the uncertainties of the measured quantities. In fact, when the measured quantities are uncorrelated, the combined uncertainty e_{comb} of a generic quantity can be computed as follows [22]:

$$e_{comb} = \sqrt{\sum_{i=1}^{n}\left(\frac{\delta f}{\delta x_i} e_{x_i}\right)^2} \tag{23}$$

where f is the combined quantity, x_i the measured ones and e_{x_i} the uncertainty associated to that quantities. To assess the partial derivative, it is essential to express the parameters as functions of the directly measured quantities, rather than derived ones. Therefore, for the combined uncertainty calculations, the formulas are expressed in terms of the read flow rate, rather than the actual flow rate. When water is adopted as single-phase fluid it is not necessary to correct the flow rate and hence the uncertainty can be directly obtained by Eq. (23) as:

$$e_{Re} = \sqrt{\left(\frac{\rho D_h}{A_f \mu} e_Q\right)^2} = \sqrt{\left(\frac{\rho Q D_h}{A_f \mu}\frac{e_Q}{Q}\right)^2} = Re\frac{e_Q}{Q} \tag{24}$$

The single-phase water uncertainty is instead obtained by applying Eq. (23) to Eq. (6) obtaining:

$$e_{f_d} = \sqrt{\left(f_D \frac{e_{\Delta P}}{\Delta P}\right)^2 + \left(2 f_D \frac{e_Q}{Q}\right)^2} \tag{25}$$

For single-phase air operations, the gas Reynolds number is expressed by combining its definition with the rotameter flow rate correction Eq. (5), obtaining the following equation:

$$Re = \frac{\frac{(P_{rot} P_{cal})^{0.5}}{R^* (T_{pl} T_{cal})^{0.5}} Q_{read} D_H}{A_f \mu} \tag{26}$$

therefore resulting in the following expression of the combined uncertainty for this dimensionless number:

$$e_{Re} = \sqrt{\left(Re\frac{e_{Q_{read}}}{Q_{read}}\right)^2 + \left(0.5 Re\frac{e_{P_{rot}}}{P_{rot}}\right)^2 + \left(0.5 Re\frac{e_{T_{Pl}}}{T_{Pl}}\right)^2} \tag{27}$$

The same approach was adopted with single-phase air friction factor resulting in the following expression of friction factor and its uncertainty:

$$f_d = \frac{2\,\Delta P\, D_H\, {A_f}^2 R^* P_{pl} T_{cal}}{P_{man} P_{cal} {Q_{read}}^2 L} \tag{28}$$

$$e_{f_d} = \sqrt{\left(2 f_d \frac{e_{Q_{read}}}{Q_{read}}\right)^2 + \left(f_d \frac{e_{P_{man}}}{P_{man}}\right)^2 + \left(f_d \frac{e_{\Delta P}}{\Delta P}\right)^2} \tag{29}$$

Regarding the two-phase analysis, the gas and liquid pressure drops needed to compute the Lockhart–Martinelli parameter and the Two-phase multiplier are computed using the measured pressure drops instead of using the friction factor correlation in order to obtain a lower uncertainty on the final values. When Eq. (23) is applied to the Lockhart–Martinelli definition (Eq. (20)) and to the Two-phase multiplier (Eq. (21)), the following combined uncertainties are obtained:

$$e_X = \sqrt{\left(0.5 X \frac{e_{\Delta P_g}}{\Delta P_g}\right)^2 + \left(0.5 X \frac{e_{\Delta P_l}}{\Delta P_l}\right)^2} \tag{30}$$

$$e_{\Phi_{TP}} = \sqrt{\left(0.5 \Phi_{TP} \frac{e_{\Delta P_{TP}}}{\Delta P_{TP}}\right)^2 + \left(0.5 \Phi_{TP} \frac{e_{\Delta P_l}}{\Delta P_l}\right)^2} \tag{31}$$

The values of minimum, maximum and average uncertainty for the different parameters is detailed in Table 4.

Table 4
Minimum, maximum and average values of expanded relative uncertainty of the main quantities.

Parameter	Expanded uncertainty		
	Min	Avg	Max
Re	2.49%	5.16%	15.00%
f_D	4.99%	12.60%	38.78%
Φ_{TP}	0.06%	0.95%	17.62%
X	0.08%	6.33%	47.78%

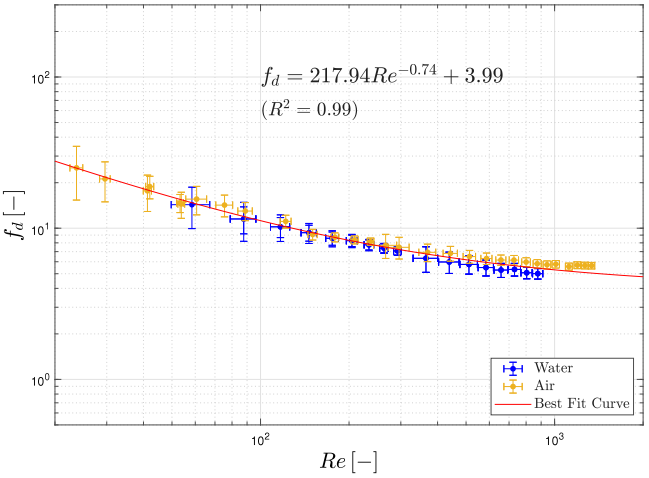

Fig. 8. Single-phase friction factor along with the best-fit curve superimposed on the single-phase measurements data.

3. Results and discussion

In this section, we present and discuss the results obtained from the experimental investigation focused on single and multiphase pressure drops, as well as the observed flow regimes and transitions in the Chevron-type plate heat exchanger (PHE). The analysis of pressure drops is of paramount importance for understanding the energy losses and hydraulic behavior of the system, while the investigation of flow regimes provides valuable insights into the flow patterns and their potential impact on heat transfer performance.

3.1. Single and two-phase pressure drop

As previously mentioned, the single-phase pressure drops were analyzed using Darcy's friction factor, as defined in Eq. (6), which correlates the pressure drop with the single-phase Reynolds number. The experimental data were fitted to a non-linear least-squares method with a curve represented by Eq. (32), where the coefficients were determined to be $A = 217.94$, $B = -0.74$, and $C = 3.99$. Fig. 8 illustrates this curve superimposed on the single-phase measurement data for both gas and liquid phases. Remarkably, the proposed function excellently interpolates the measured data points, leading to a high R^2 value close to unity.

$$f_D = ARe^B + C \tag{32}$$

The correlation is able to predict the experimental data with a Mean Percentage Error (MPE) of 0.34% and a Mean Absolute Percentage Error (MAPE) of 5.23%. In Fig. 9 the pressure drop measured experimentally and the one computed using the interpolated correlation are reported on the parity plot.

Fig. 10 shows instead the comparison between the proposed correlation for single-phase friction factor and the ones available in literature given by different authors. The details about the geometry investigated by these authors, the proposed correlations as well as the Re number

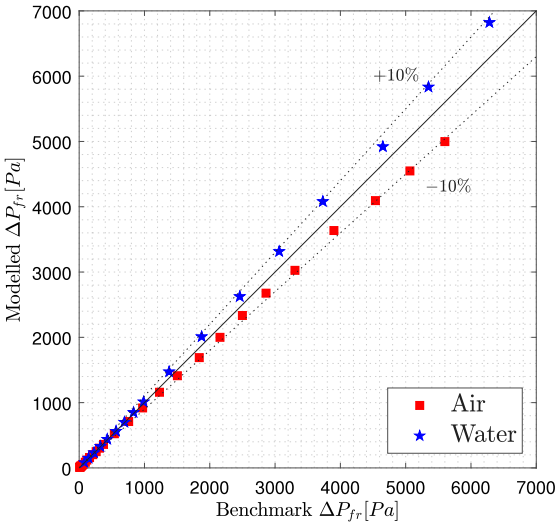

Fig. 9. Accuracy of the single-phase pressure drop correlation.

range of validity are summarized in Table 5. The reference works were chosen according to the ones that have similar geometrical characteristics to the plates considered in the present work. This concept can be summarized with a similar area enlargement factor, which refers to the ratio of the total heat transfer surface area of the exchanger to the projected planar area of the plates. It is clearly visible how all the different correlations exhibit about the same trend, and also correlation proposed in this work aligns well with it. The friction factor predicted by present correlation is close to the one computed with Gulenoglu [23], Huang [24] and Warnakulasuriya [25]. The friction factors predicted by Grabenstein [14], Muley [26,27] and Arsenyeva [28] are instead much lower, this proves that the choice of a correlation for single phase pressure drop in PHEs is a quite delicate matter and even for the same geometrical parameters high deviations in results can be expected. The high variability of literature correlation predictions demonstrates that the development of a correlation that captures the behavior of the present system when operated in single phase was a necessary preliminary step in order to conduct the following two-phase analysis.

In relation to the two-phase pressure drop analysis, Fig. 11 presents the correlation between the Two-Phase Multiplier Φ_{TP} and the Lockhart–Martinelli parameter X. After a preliminary analysis in which homogeneous models for pressure drops were evaluated, it was chosen to adopt only the Lockhart–Martinelli separated flow approach. The homogeneous models considered gave noncorrelatable results, the only model worth mentioning is Dukler's model [30] that only worked when applied to mass fluxes higher than 50 $\frac{kg}{m^2\ s}$ and volume qualities higher than 0.8. The experimental data for estimating the void fraction using the homogeneous model are depicted in Fig. 11(a), while Fig. 11(b) shows the results obtained using the proposed drift-flux model based on Asano's data [17,18]. Since Lockhart and Martinelli [20] observed that in pipes the two-phase multiplier is dependent only on the Lokhart–Martinelli parameter and is not influenced by the liquid flow rate, it is expected that the same behavior should be observed in PHEs. Authors [11,14,17,31] that preferentially investigated only the high flux region where the gravitational component has a minor impact on the global pressure drop, obtained results that confirm this hypothesis for PHEs. Two-phase multiplier data points should have a very low dispersion and collapse on a single interpolant curve. In our analysis, this can be appreciated only when applying the Drift flux void fraction model. The difference between the two approaches is significant. The homogeneous model tends to considerably overestimate the void fraction, particularly at low water flow rates, resulting in differences from the drift-flux model that can exceed 100%. Consequently, this

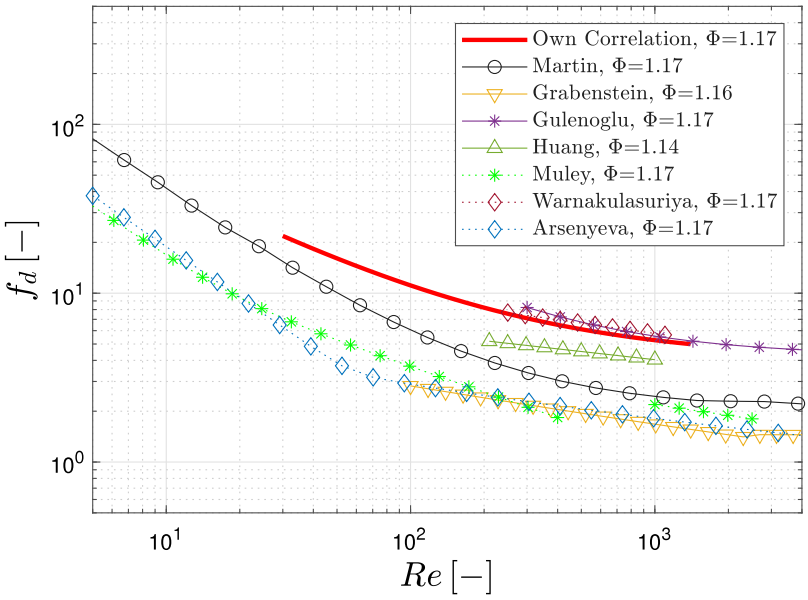

Fig. 10. Comparison between various single-phase friction factor correlations for similar area enlargement factor (Φ) values. The curves were plotted based on the geometrical parameters of the present study: b_p = 2.5 mm, λ = 9 mm, φ = 63°.

Table 5
Summary of the single-phase friction factor correlations proposed in Fig. 10.

Author	Correlation	Re range	Angle [°]	Φ [–]	b_p [mm]	λ [–]
Martin [29]	$f_D = \left(\frac{cos(\varphi)}{\sqrt{0.18\tan(\varphi)+0.36\sin(\varphi)+f_0(Re)/cos(\varphi)}} + \frac{1-cos(\varphi)}{\sqrt{3.6 f_{1,0}}}\right)^{-2}$ $f_0 = \frac{64}{Re}$ $f_{1,0} = \frac{597}{Re} + 3.85$ $f_0 = (1.8 log10(Re) - 1.5)^{-2}$ $f_{1,0} = \frac{39}{Re^{0.289}}$	$Re < 2000$ $Re > 2000$	0° < φ < 80°	[–]	[–]	[–]
Grabenstein et al. [14]	$f_D = 8.67 Re^{-0274} + 0.37$ $f_D = 1.49 Re^{-0.00326}$	Re < 2300 Re > 2300	63	1.155	3	11.4
Gulenoglu et al. [23][a,b]	$f_D = (1039(\Phi Re)^{-0.9227} + 4.984)/\Phi$	300 < Re < 5000	60	1.17	2.76	10
Huang [24]	$f_D = 12.28 Re^{-0.161}$	210 < Re < 1000	60	1.14	2	8.1
Muley et al. [26,27][a,b]	$f_D = \frac{4}{\Phi}((30.2/(\Phi Re))^5 + (6.28/(\Phi Re)^{0.5})^5)^{0.2} \cdot (\frac{\varphi}{30})^{0.83}$ $f_D = \frac{4}{\Phi}[(2.917 - 0.1277\varphi + 2.016 \cdot 10^{-3}\varphi^2) \cdot (\Phi Re)^{-(0.2+0.0577 sin(\frac{\varphi g}{45}+2.1))}]$	2 < Re < 300 Re > 1000	30 < φ < 60 30 < φ < 60	1.174[c]	2.5	9
Warnakulasuriya et al. [25]	$f_D = 23.8 Re^{-0.205}$	250 < Re < 1100	60	1.17	2.5	10.2
Arsenyeva et al. [28][b]	$f_D = \frac{8}{\Phi} \cdot \left[\left(\frac{12+\frac{\pi\varphi/2}{3}}{\Phi Re}\right)^{12} + \left(A + \left(\frac{37530\exp(-0.157\varphi)}{\Phi Re}\right)^{16}\right)^{-\frac{3}{2}}\right]^{\frac{1}{12}}$ $A = \left[p \cdot \ln\left(\frac{1+0.1\varphi}{(\frac{7}{\Phi Re}\cdot\exp(-\pi\cdot\frac{\varphi}{180}\cdot\frac{1}{\gamma^2}))^{0.9}+0.27\cdot10^{-5}}\right)\right]^{16}$ $p = \left(0.061 + \left(0.69 + \tan\left(\varphi\frac{\pi}{180}\right)\right)^{-2.63}\right) \cdot (1 + (1-\gamma)\cdot 0.9 \cdot \varphi^{0.01})$ $\gamma = \frac{2b_p}{\lambda}$	5 < Re < 25000	14° < φ < 72°	1.15 < Φ < 1.49	[–]	[–]

[a] The original correlation is for Fanning friction factor and is hereby converted to Darcy friction factor.
[b] The original correlation adopts equivalent diameter for expressing Re and f_D, and is hereby converted in order to adopt the hydraulic diameter.
[c] The author originally reports Φ = 1.29 but according to the definition provided in this manuscript and the geometrical details provided in [26,27] it results Φ = 1.174.

leads to an underestimation of the gravitational pressure drop and an overprediction of the frictional two-phase pressure drop, causing an increase in the predicted Φ_{TP} at constant X. These findings highlight the importance of using an accurate void fraction model, as it significantly impacts the predictions of two-phase pressure drops and flow behavior within the plate heat exchanger.

The curve that best fit the data is proposed in the form presented by Chisholm in [21] where the Lockhart–Martinelli parameter and multiplier are correlated in the form of Eq. (33).

$$\Phi_{TP}^2 = 1 + \frac{C}{X} + \frac{1}{X^2} \tag{33}$$

Considering the data processed with the new model for void fraction, the coefficient C is equal to 8.77, a value in between 5 and 10 which are the two limit values for viscous–viscous and turbulent–viscous flow in circular pipes as suggested by Chisholm himself [21]. In order to provide a benchmark against other experimental works, Fig. 12

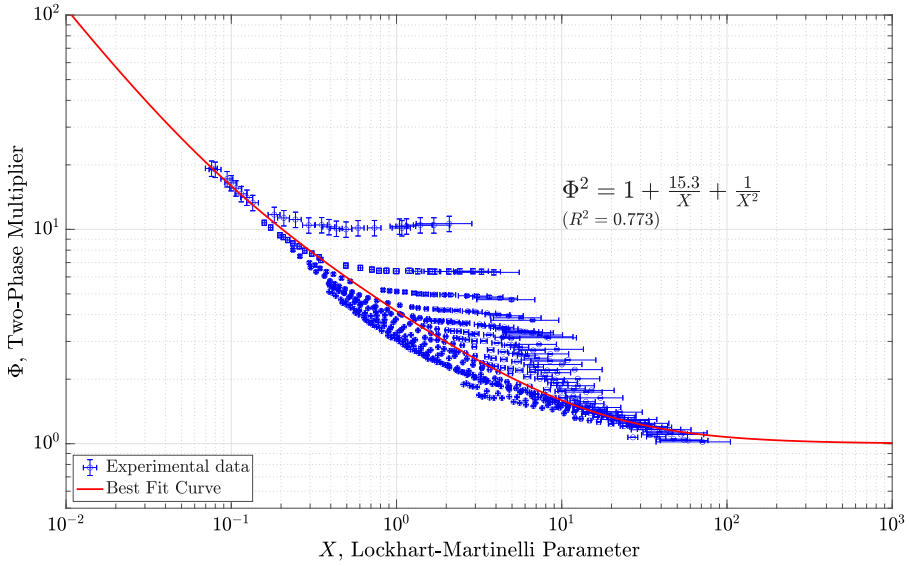

(a) Homogeneous model

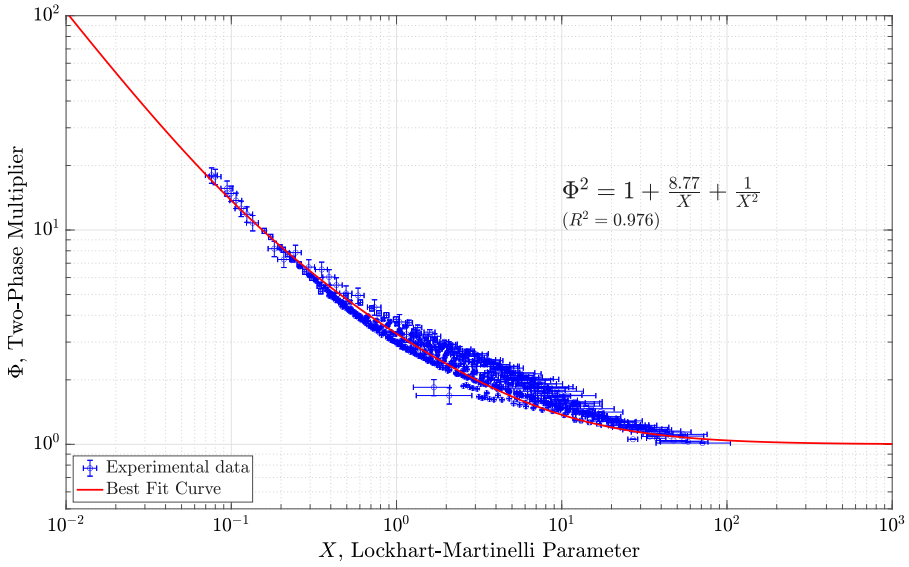

(b) Drift flux model

Fig. 11. Lockhart–Martinelli plots applying two different model for void fraction estimation.

display the experimental data superimposed to different correlations available in literature as well as the one proposed in this work. To guarantee direct comparability, the works chosen as benchmark adopt the same operating fluid (air and water mixture) and have very similar corrugation geometry. It is clearly noticeable how our data processed with the proposed drift-flux model are entirely in between the range defined by the different correlations. This outcome supports the validity of the correlation and the predictive capability of the model derived from the experimental data. Moreover, to show the superior accuracy of the model proposed when using the drift flux-based model for void fraction estimation, a parity plot is shown in Fig. 13. Here the modeled frictional pressure drops are compared against the experimental data. When making the homogeneous flow assumption, the Mean Average Percentage Error (MAPE) of the prediction is 38.9% while it is 20.5% for the other case (see Table 6).

3.2. Flow visualization

The primary objective of the visualization campaign was to establish a clear and consistent classification of the various flow patterns observed in a Chevron-type corrugated channel operated in the upward configuration. While flow patterns in pipes are well-established and universally recognized, the nomenclature for Plate Heat Exchangers (PHEs) lacks uniformity, with different studies using diverse terms to describe the same patterns. In line with the approach proposed by Buscher in [15], the researchers categorized the visualized flow regimes into five main patterns: bubbly flow, film flow, Taylor-like flow, heterogeneous flow, and partial film. The last three patterns were grouped together and referred to as transition flows. This classification aims to provide a comprehensive and consistent framework for characterizing the observed flow patterns in PHEs.

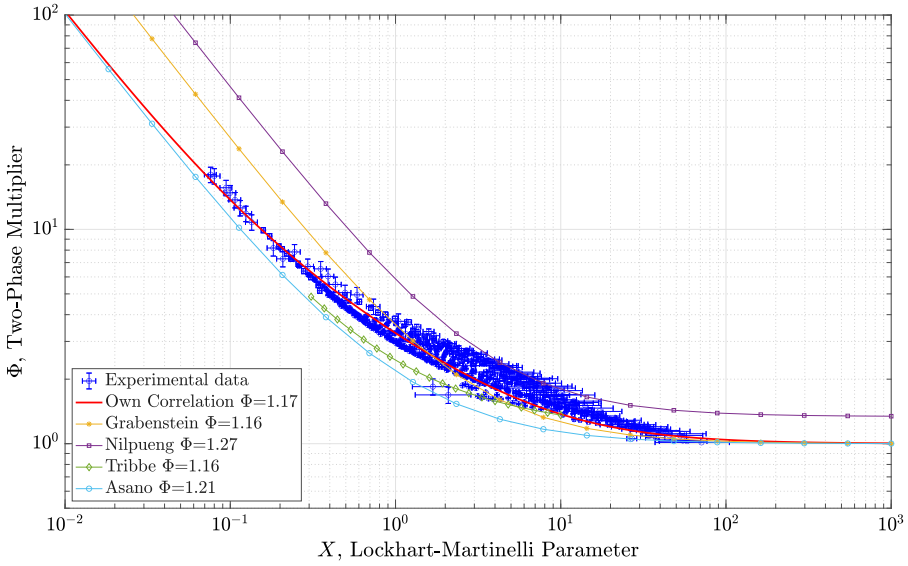

Fig. 12. Comparison between different correlation for two-phase multiplier Lockhart–Martinelli parameter.

Table 6
Summary of the Lockhart–Martinelli correlations proposed in Fig. 12.

Author	Correlation	Angle [°]	Φ [–]	b_p [mm]	λ [–]
Grabenstein et al. [14]	$1 + 2.57/X$	63	1.155	3	11.4
Nilpueng et al. [31]	$1.339 + 4.492/X$	Mixed 80–35	1.27	2.5	7
Tribbe et al. [11]	$1.423 - 0.0724\ln(X) + 1.031X$	60	1.117	3	13.25
Asano et al. [17]	$(1 + 2.73/X + 1/X^2)^{0.5}$	Not reported	1.21	2.5	8

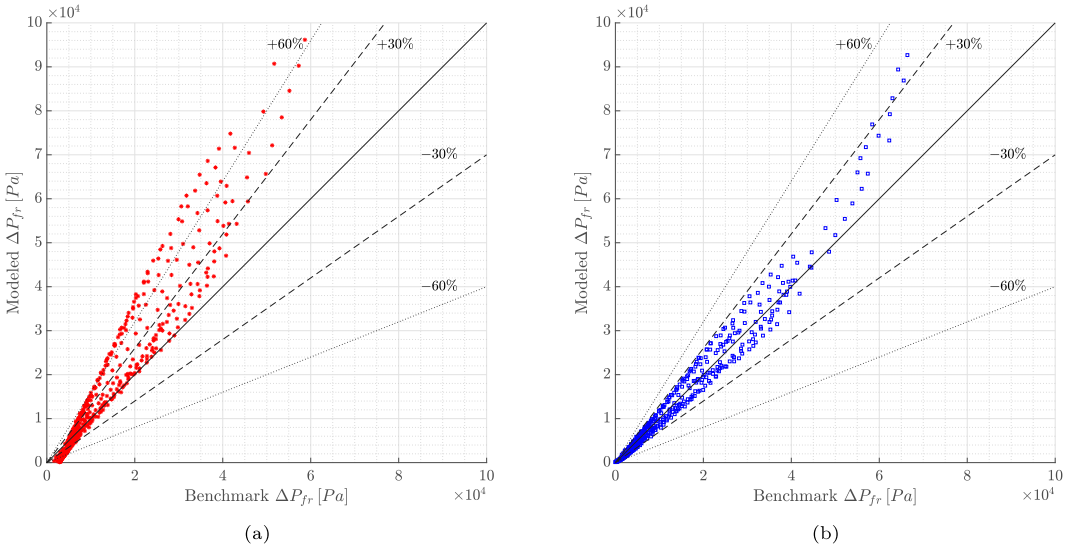

Fig. 13. Accuracy of the proposed model against measured frictional pressure drop when using homogeneous flow hypothesis (a) or the proposed drift flux model (b) for the estimation of the void fraction.

Bubbly flow refers to a fluid flow characterized by the presence of gas bubbles dispersed within the liquid phase. It can be further classified into two categories: *fine* and *coarse* bubbly flows. The size of the bubbles in a bubbly flow is primarily influenced by the phenomena of bubble coalescence and break-up. The energy dissipation rate plays a crucial role in determining the dimension of the bubbles: higher energy dissipation results in smaller bubble diameters, leading to a fine bubbly flow. On the other hand, when the turbulence is insufficient to create bubbles smaller than the corrugations, the dominant mechanism is bubble coalescence, resulting in a coarse bubbly flow. Figs. 14(a) and 14(b) provide visual representations of these flow patterns.

Film flow in Plate Heat Exchangers (PHEs) exhibits similarities to annular flow observed in tubes, where a thin layer of liquid flows along the channel walls while the majority of the cross-sectional area is occupied by gas. Notably, Vlasogiannis et al. [13] observed that the liquid flows in a valley pattern, reversing direction at the channel edges. However, as the gas velocity increases, the liquid takes on a spiral shape with reversals occurring at contact points. At these points, pockets of liquid form due to the combined effects of surface tension and adhesion to the walls. Nevertheless, it is essential to note that at extremely high gas flow rates, certain areas of the channel may experience partial drying out. Fig. 15(d) provides an illustration of this flow pattern in a PHE configuration.

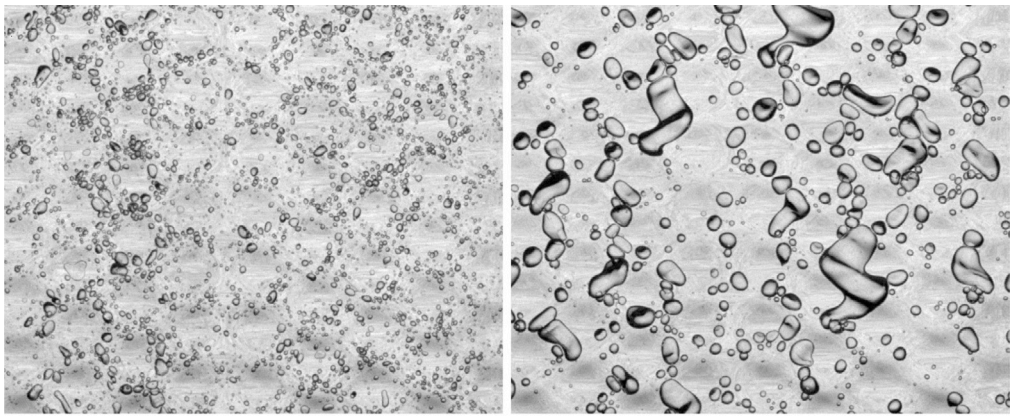

Fig. 14. Example of fine (a) and coarse (b) bubbly flow. Pictures from experiments.

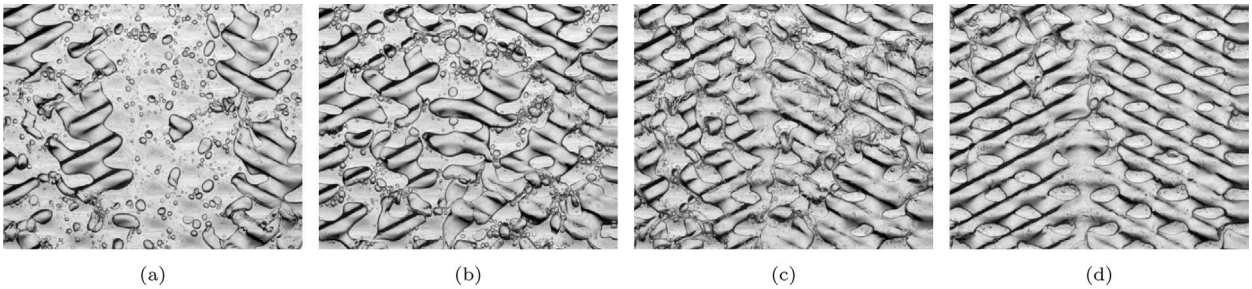

Fig. 15. Example of transition flow pattern: (a) Taylor-like, (b) Heterogeneous flow, (c) Partial film flow and (d) Film flow. Pictures from experiments. Gas flow rate increasing from left to right.

Transition flows represent the intermediate patterns observed between bubbly and film flow in Plate Heat Exchangers (PHEs). As the gas flow rate increases, the bubbles within the plate's cross-section become larger and adopt an irregular zigzag shape, known as *Taylor-like* bubbles. With further increases in the gas flow rate, Taylor-like bubbles become wider, more frequent, and start to entrap liquid regions. If the gas patches are distinguishable and surrounded by gas bubbles, the flow pattern is identified as *heterogeneous flow*. On the other hand, if the entrapped liquid is limited to contact points, and the gas patches are the predominant flow structure, but not stable enough to form a full film flow, the regime is termed *partial film flow*. This transition between regimes occurs gradually, and with further increases in the gas flow rate, a stable film flow may be observed. Examples of these transition flow patterns are visually represented in Fig. 15.

All the visualized experimental points have been classified into the discrete categories defined previously, and the resulting flow regime map is presented in Fig. 16. It is evident from this map that the transitions between different patterns occur gradually. Specifically, fine bubbly flow is observed only above a certain water flow rate. Additionally, at very high flow rates of both phases, a few points were classified as "unstable" due to pressure oscillations in the corrugated channel, which hindered the clear definition of a specific flow regime.

3.3. Flow pattern transition criteria

The task of predicting the transition between flow regimes is non-trivial. Typically, studies about flow visualization always comprehend a discussion about this topic. By looking at the visual-based classification of flow pattern reported in the previous section and specifically displayed in Fig. 16, it is noticeable how the transition between the principal patterns occurs along well-defined boundaries. As suggested by Buscher in [15], the transition between coarse and fine bubbly flow was modeled on the basis of turbulent kinetic energy induced breakage. For such conditions Hinze [32] calculated the maximum bubble diameter as function of fluid properties and turbulent kinetic energy dissipation rate ϵ:

$$d_{max} = K \left(\frac{\sigma}{\rho_L} \right)^{\frac{3}{5}} \epsilon^{-\frac{2}{5}} \tag{34}$$

$$K = 0.725 + 4.15\,\alpha^{0.5} \quad \text{(Calderbank expression)} \tag{35}$$

Hinze's [32] formulation was derived under the hypothesis of isotropic and homogeneous turbulence. The assumption of isotropic turbulence structures is relaxed by Hinze himself to the isotropy of only the microscale structures; such a condition is also commonly observed in presence of strongly non-isotropic macrostructures like the ones observed in PHEs. Instead, the homogeneous turbulence condition cannot be expected due to the geometry of the PHEs. Contact points between plates promote a strongly inhomogeneous flow field in the channel by creating recirculation regions behind them. In light of these assumptions, even though the second one is not clearly verified, Hinze's model still gives a reasonable prediction of maximum bubble diameter which is a good starting point for an empirical fitting. Taitel [33] approximated the turbulent kinetic energy (ϵ) dissipation rate as:

$$\epsilon = \left| \frac{dP}{dz} \right| \frac{J}{\rho_m} \tag{36}$$

The hereby derived model for two-phase frictional pressure gradient was used to estimate the frictional pressure gradient in the previous equation by adopting Eq. (22) in differential form and the correlation for the two-phase multiplier:

$$\left(\frac{dP}{dz} \right)_{TP} = \Phi_{TP}^2 \left(\frac{P}{dz} \right)_l = \left(1 + \frac{8.77}{X} + \frac{1}{X^2} \right) \frac{1}{2} f_d \frac{\rho_L v_{s,L}^2}{D_h} \tag{37}$$

Moreover, the transition between fine and coarse was assumed to occur when bubbles diameter exceed a given percentage of the hydraulic

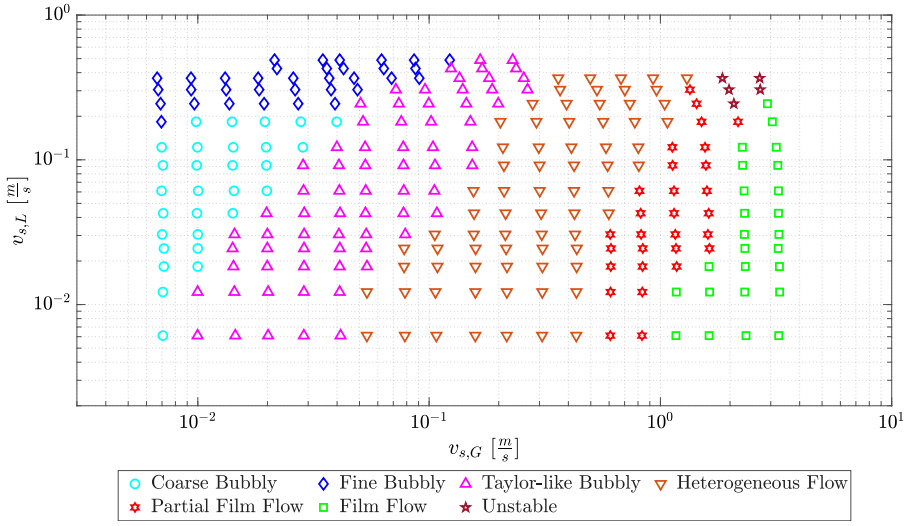

Fig. 16. Flow regime map of the visualized data.

Table 7
Summary of the fitted parameters to define the transition lines.

Pattern 1	Pattern 2	Fitting parameter	Value
Coarse Bubbly	Fine Bubbly	M	0.50
Coarse Bubbly	Taylor-like Bubbly	α	0.06
Fine Bubbly	Taylor-like Bubbly	α	0.10
Taylor-like Bubbly	Heterogeneous Flow	α	0.25
Heterogeneous Flow	Partial Film Flow	α	0.50
Partial Film Flow	Film Flow	α	0.56

diameter, represented by parameter M:

$$d_{max} = M D_h = M \frac{2b_p}{\Phi} \tag{38}$$

Combining the Eq. (34), (36) and (38) it is possible to find an expression for mixture velocity dependant on the parameters just introduced:

$$J = \left(\frac{K\Phi}{2b_p M}\right)^{\frac{5}{2}} \left(\frac{\sigma_L}{\rho_L}\right)^{\frac{3}{2}} \frac{\rho_m}{\left|\frac{dP}{dz}\right|} \tag{39}$$

Using an iterative procedure where gas superficial velocity was first guessed and the corrected for each liquid velocity until convergence, we determined the transition line separating fine and coarse bubble flow depending on the parameter M. This was then fit according to our data and transition was found to occur when the bubble size is less than 50% of the hydraulic diameter, corresponding to a value of $M = 0.5$.

The transitions between the other flow pattern were all modeled as occurring at constant void fraction. For this reason, the drift flux model in Eq. (18) was rearranged in order to find a relation between liquid and gas superficial velocities for constant void fraction:

$$\begin{aligned} \frac{v_{s,G}}{\alpha} &= U_g = C_0\, J + U_{gj} = C_0\, \left(v_{s,G} + v_{s,L}\right) + U_{gj} \\ &\implies C_0\, v_{s,L} = \frac{v_{s,G}}{\alpha} - C_0\, v_{s,G} - U_{gj} \\ v_{s,L} &= \frac{v_{s,G}}{C_0\,\alpha} - v_{s,G} - \frac{U_{gj}}{C_0} = \frac{1 - C_0\,\alpha}{C_0\,\alpha}\, v_{s,G} - \frac{U_{gj}}{C_0} \end{aligned} \tag{40}$$

The void fraction values were then computed with the model derived from Asano's data. To summarize, Table 7 are reports the values of void fraction and M parameter obtained by the fitting of the transition lines.

In Fig. 17 the hereby defined transition lines are displayed on the flow map. The proposed transition lines well-fit the visually observed flow regimes. At low liquid velocities though, a deviation of the transition from the iso-void fraction line is observed. This could be due to the impact of the void fraction model adopted. In fact the data from Asano's work [17,18] do not provide many detail for low mixture velocities having the first data point at about $J = 0.5$ m/s. Additionally, for very low liquid flow rates, gas stagnation in front of the contact points was observed and this could have influenced the void fraction distribution in the corrugated channel. It is worth noticing that overlayed lines of constant volume fraction (x_v) fail in predicting the transitions as the exhibit a completely different trend. This underlines the importance of defining a good void fraction model to improve the prediction of flow pattern transitions.

In Table 8 few metrics to assess the prediction accuracy of the newly defined transition lines are shown. The experimental data point were classified four categories: True Positive (TP), True Negative (TN), False Positive (FP) and False Negative (FN). Looking at each flow pattern region once at a time, a point is classified as TP if its experimentally determined flow pattern agrees with the one predicted by the proposed transition line. It is a FP instead if it lies inside the region of a particular regime but it was experimentally classified as another one. On the other hand, a FN is a point that was classified as the pattern of interest but it resides in the region of a neighboring pattern. True negatives of each flow pattern are then computed as the total number of point minus the sum of specific TP, FP and FN points. Given this classification is possible to compute some general metrics used to assess the quality of prediction model such as accuracy, precision and recall. The first accounts for the portion of correct prediction, the second expresses the proportion of true positive predictions among all positive predictions and the latter instead the proportion of true positive predictions among all actual positive pixels. The mathematical definition of these three metrics is given below.

$$\text{Accuracy} = \frac{TP + TN}{TP + TN + FP + FN} \tag{41}$$

$$\text{Precision} = \frac{TP}{TP + FP} \tag{42}$$

$$\text{Recall} = \frac{TP}{TP + FN} \tag{43}$$

Overall the prediction of flow patterns is quite accurate. In view of these results, criteria based on constant void fraction seem to be effective for predicting flow patterns. To further improve accuracy, priority should be given to developing more precise void fraction models.

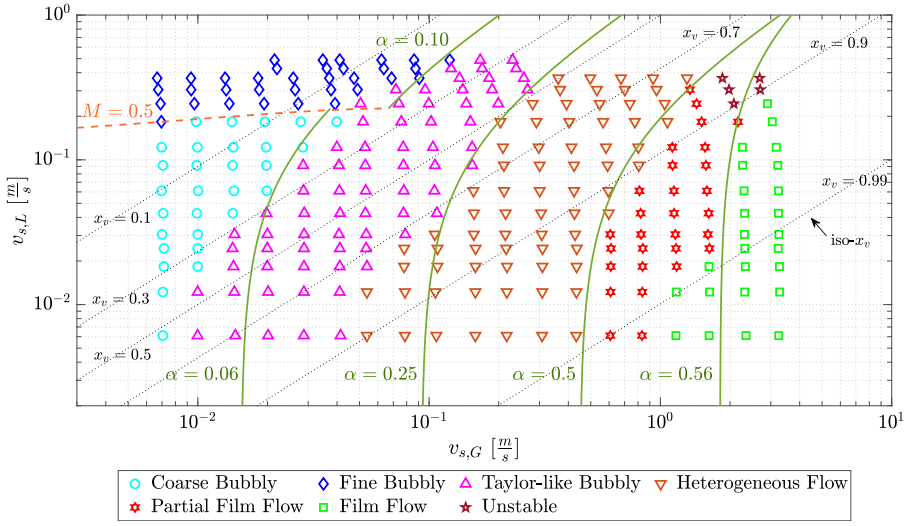

Fig. 17. Flow regime map with transition lines.

Table 8
Metrics to assess the predictive accuracy of the transition lines.

	Fine	Coarse	Taylor	Heterogeneous	Partial F.	Film	Average
N° Exp. Points	34	29	70	71	29	25	
Accuracy	98.4%	96.5%	93.0%	95.7%	96.5%	97.7%	96.3%
Precision	94.1%	79.4%	87.1%	98.4%	77.8%	95.2%	88.7%
Recall	94.1%	93.1%	87.1%	85.9%	96.6%	80.0%	89.5%

4. Conclusions

In this study, we investigated two-phase flow in a Chevron-type corrugated channel. The experimental work focused on measuring single-phase and two-phase pressure drops, as well as visualizing the two-phase flow regimes. The test facility consisted of two transparent corrugated plates with a corrugation angle of 63°, enclosed in a steel frame to maintain contact. To ensure homogeneity of the injection, an air–water mixture was supplied via a mixing plenum. The loop was operated in adiabatic conditions. High-speed cameras were used for flow visualization.

For single-phase flow, pressure drops were measured and a dimensionless analysis was performed, leading to a novel correlation for Darcy's friction factor. To predict void fraction and extract frictional pressure drop from the measured total ones, a new model based on Drift-Flux analysis on the data proposed by Asano et al. [17,18] was introduced. Two-phase pressure drops were then represented using two-phase multipliers on Lockhart–Martinelli plots. The newly proposed void fraction model outperformed the homogeneous flow assumption, resulting in less scattered and better correlated data. Additionally, the accuracy of the two-phase pressure drop model was significantly improved.

The visualization campaign yielded a comprehensive classification of different flow patterns in the corrugated channel of a plate heat exchanger. Three main flow patterns were identified as bubbly, transition, and film flow, with various sub-categories observed under different operating conditions, such as fine/coarse bubbly flow and Taylor-like/heterogeneous/partial film transition flow. By applying the developed void fraction and pressure drop models, new criteria for flow pattern transitions were defined, enabling accurate flow pattern predictions. Overall, this work provides valuable insights into the behavior of two-phase flow in a Chevron-type corrugated channel contributes to the understanding and provide correlation and insights that could be useful for the design and optimization of compact plate heat exchangers.

CRediT authorship contribution statement

Stefano Passoni: Writing – review & editing, Writing – original draft, Visualization, Validation, Methodology, Investigation, Formal analysis, Data curation, Conceptualization. **Andrea Ferrario:** Writing – review & editing, Writing – original draft, Investigation, Formal analysis, Data curation. **Marco E. Ricotti:** Project administration, Funding acquisition, Conceptualization. **Riccardo Mereu:** Writing – review & editing, Supervision, Methodology, Conceptualization.

Declaration of competing interest

The authors declare the following financial interests/personal relationships which may be considered as potential competing interests: Stefano Passoni reports financial support was provided by EU Framework Programme for Research and Innovation Euratom.

Data availability

Data will be made available on request.

Acknowledgments

This work has received funding from the Euratom research and training programme 2014–2018 under Grant Agreement No. 847553.

Appendix A

With the approximation adopted in this paper the mean channel height is assumed to be equal to one corrugation depth. This can be proved integrating the channel shape over the channel width, but having each channel a sinusoidal shape it can be computed as two times the frontal area of the semi-channel. Hence the frontal area is:

$$A_f = 2\int_0^{B_p} \frac{b_p}{2}\left(1+\sin\left(\frac{2\pi x}{\lambda_n}\right)\right)dx = b_p\left[x-\frac{\lambda_n}{2\pi}\cos\left(\frac{2\pi x}{\lambda_n}\right)\right]_0^{B_p} = b_p B_p + \frac{\lambda_n b_p}{2\pi}\left(1-\cos\left(\frac{2\pi B_p}{\lambda_n}\right)\right) \quad (A.1)$$

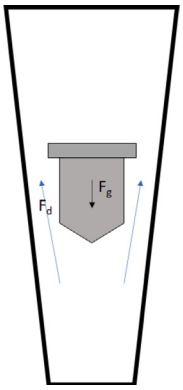

Fig. B.18. Geometry of the rotameter.

In this present equation B_p is the channel width, b_p the corrugation depth, λ_n the wavelength of the corrugation profile perpendicular to the flow direction that can be computed from the geometric corrugation wavelength and corrugation angle as $\frac{\lambda}{\cos(\theta)}$. The frontal area can be rewritten as:

$$A_f = b_p B_p \left(1 + \frac{\lambda_n}{2\pi B_p}\left(1 - \cos\left(\frac{2\pi B_p}{\lambda_n}\right)\right)\right) \tag{A.2}$$

Hence the relative error due to approximation of the frontal area as the product between corrugation height and channel width is given by:

$$\frac{\lambda_n}{2\pi B_p}\left(1 - \cos\left(\frac{2\pi B_p}{\lambda_n}\right)\right) < \frac{\lambda_n}{2\pi B_p}(1-(-1)) = \frac{\lambda_n}{\pi B_p} = \frac{\lambda}{\pi B_p \cos(\theta)} \tag{A.3}$$

In present configuration λ=9 mm, B_p=182 mm and θ=63°, therefore it can be stated that the error is certainly less than 3.4%.

Appendix B

To accurately measure the flow rate, it is necessary to apply a correction to the rotameter reading. This is due to the operating conditions that are commonly different from the ones at which the instrument is calibrated. The formulation of Eq. (5) is obtained by a balance of forces on the float of the instrument, and is necessary when operated with gases. Rotameters are characterized by an increasing cross-section along the axial coordinate, Fig. B.18 displays the instrument's geometry. The float is kept suspended by the drag force that is determined by gas velocity and has to be equal to its weight force. For this reason, there is a precise axial coordinate for which the float is at equilibrium. From the force balance:

$$\frac{1}{2}\rho_f C_d A_{fl} \frac{Q^2}{A_r^2} = M_{fl}\, g \tag{B.1}$$

$$Q = \sqrt{\frac{2\, M_{fl}\, g\, A_r^2}{\rho_f\, C_d\, A_{fl}}} \tag{B.2}$$

where ρ_f is the fluid density, C_d the drag coefficient, A_{fl} the float frontal area, Q the volumetric flow rate, A_r the rotameter section, M_{fl} the mass of the float and g the gravitational constant. The rotameter graduated scale is determined during calibration and hence the reading is correct only if the instrument is operated at the same conditions. In other cases, the same reading indicates a different flow rate. In this condition, from Eq. (B.2), it can be noticed that given the cross-section A_r, only the density varies on the right hand side of the equation, and it can be written:

$$\sqrt{\rho_f} Q = const \tag{B.3}$$

$$\sqrt{\rho_{f,cal}} Q_{read} = \sqrt{\rho_{f,rot}} Q_{rot} \tag{B.4}$$

where the subscript *cal* stands for "during calibration", *rot* stands for "at rotameter actual conditions" and *read* stands for "reading". Under the approximation of ideal gas, the density can be expressed simply as function of pressure and temperature:

$$\rho = \frac{P}{R^* T} \tag{B.5}$$

leading to

$$Q_{rot} = \sqrt{\frac{\rho_{f,cal}}{\rho_{f,rot}}} Q_{read} = \sqrt{\frac{P_{cal}}{P_{rot}}}\sqrt{\frac{T_{rot}}{T_{cal}}} Q_{read} \tag{B.6}$$

Since the quantity of interest is the actual flow rate through the channel, one may retrieve the correct quantity from a mass balance (Eq. (B.7)) considering that the flow is adiabatic and the temperature of the rotameter is the same as the one of the plate ($T_{rot} = T_{pl}$). This results in Eq. (B.8) that coincides with Eq. (5).

$$\rho_{pl} Q_{pl} = \rho_{rot} Q_{rot} \tag{B.7}$$

$$Q_{pl} = \frac{\rho_{rot}}{\rho_{pl}} Q_{rot} = \frac{P_{rot}}{P_{pl}} Q_{rot} = \frac{\left(P_{rot} P_{cal}\right)^{0.5}}{P_{pl}} \left(\frac{T_{pl}}{T_{cal}}\right)^{0.5} Q_{read} \tag{B.8}$$

References

[1] J. Kang, J.Y. Bak, B.J. Lee, C.K. Chung, B. Yun, Numerical investigation of a plate-type steam generator for a small modular nuclear reactor, Nucl. Eng. Technol. 54 (2022) 3140–3153, http://dx.doi.org/10.1016/j.net.2022.02.020.
[2] Z.H. Ayub, Plate heat exchanger literature survey and new heat transfer and pressure drop correlations for refrigerant evaporators, Heat Transf. Eng. 24 (5) (2003) 3–16, http://dx.doi.org/10.1080/01457630304056.
[3] H. Martin, N6 pressure drop and heat transfer in plate heat exchangers, in: VDI Heat Atlas, Springer Berlin Heidelberg, Berlin, Heidelberg, 2010, pp. 1515–1522, http://dx.doi.org/10.1007/978-3-540-77877-6_109.
[4] K. Thulukkanam, Heat Exchanger Design Handbook, CRC Press, 2000.
[5] S. Kakaç, H. Liu, A. Pramuanjaroenkij, Heat Exchangers: Selection, Rating, and Thermal Design, second ed., in: Designing for Heat Transfer, Taylor & Francis, 2002.
[6] L. Wang, B. Sundén, R. Manglik, Plate Heat Exchangers: Design, Applications and Performance, in: Developments in Heat Transfer, WIT Press, 2007.
[7] J. Klemes, O. Arsenyeva, P. Kapustenko, L. Tovazhnyanskyy, Compact Heat Exchangers for Energy Transfer Intensification: Low Grade Heat and Fouling Mitigation, Taylor & Francis Group, 2017.
[8] Z.H. Ayub, T.S. Khan, S. Salam, K. Nawaz, A.H. Ayub, M. Khan, Literature survey and a universal evaporation correlation for plate type heat exchangers, Int. J. Refrig. 99 (2019) 408–418, http://dx.doi.org/10.1016/j.ijrefrig.2018.09.008.
[9] R.L. Amalfi, F. Vakili-Farahani, J.R. Thome, Flow boiling and frictional pressure gradients in plate heat exchangers. Part 1: Review and experimental database, Int. J. Refrig. 61 (2016) 166–184, http://dx.doi.org/10.1016/j.ijrefrig.2015.07.010.
[10] R. Eldeeb, V. Aute, R. Radermacher, A survey of correlations for heat transfer and pressure drop for evaporation and condensation in plate heat exchangers, Int. J. Refrig. 65 (2016) 12–26, http://dx.doi.org/10.1016/j.ijrefrig.2015.11.013.
[11] C. Tribbe, H.M. Müller-Steinhagen, Gas/liquid flow in plate-and-frame heat exchangers - Part II: Two-phase multiplier and flow pattern analysis, Heat Transf. Eng. 22 (2001) 12–21, http://dx.doi.org/10.1080/01457630150215686.
[12] C. Tribbe, H.M. Müller-Steinhagen, Gas/liquid flow in plate-and-frame heat exchangers - Part I: Pressure drop measurements, Heat Transf. Eng. 22 (1) (2001) 5–11, http://dx.doi.org/10.1080/01457630118144.
[13] P. Vlasogiannis, G. Karagiannis, P. Argyropoulos, V. Bontozoglou, Air–water two-phase flow and heat transfer in a plate heat exchanger, Int. J. Multiph. Flow 28 (2002) 757–772, http://dx.doi.org/10.1016/S0301-9322(02)00010-1.
[14] V. Grabenstein, A.E. Polzin, S. Kabelac, Experimental investigation of the flow pattern, pressure drop and void fraction of two-phase flow in the corrugated gap of a plate heat exchanger, Int. J. Multiph. Flow 91 (2017) 155–169, http://dx.doi.org/10.1016/j.ijmultiphaseflow.2017.01.012.
[15] S. Buscher, Visualization and modelling of flow pattern transitions in a cross-corrugated plate heat exchanger channel with uniform two-phase distribution, Int. J. Heat Mass Transfer 144 (2019) 118643, http://dx.doi.org/10.1016/j.ijheatmasstransfer.2019.118643.
[16] S. Buscher, Two-phase pressure drop and void fraction in a cross-corrugated plate heat exchanger channel: Impact of flow direction and gas-liquid distribution, Exp. Therm Fluid Sci. 126 (2021) 110380, http://dx.doi.org/10.1016/j.expthermflusci.2021.110380.
[17] H. Asano, N. Takenaka, T. Fujii, Flow characteristics of gas-liquid two-phase flow in plate heat exchanger (Visualization and void fraction measurement by neutron radiography), Exp. Therm Fluid Sci. 28 (2004) 223–230, http://dx.doi.org/10.1016/S0894-1777(03)00043-8.

[18] H. Asano, N. Takenaka, T. Wakabayashi, T. Fujii, Visualization and void fraction distribution of downward gas–liquid two-phase flow in a plate heat exchanger by neutron radiography, Nucl. Instrum. Methods Phys. Res. A 542 (2005) 154–160, http://dx.doi.org/10.1016/j.nima.2005.01.093.

[19] N. Zuber, J.A. Findlay, Average volumetric concentration in two-phase flow systems, J. Heat Transfer 87 (4) (1965) 453–468, http://dx.doi.org/10.1115/1.3689137.

[20] W. Lockhart, Proposed correlation of data for isothermal two-phase, two-component flow in pipes, Chem. Eng. Prog. 45 (1) (1949) 39–48.

[21] D. Chisholm, A theoretical basis for the Lockhart-Martinelli correlation for two-phase flow, Int. J. Heat Mass Transfer 10 (12) (1967) 1767–1778.

[22] Joint Committee for Guides in Metrology, JCGM 100: Evaluation of Measurement Data - Guide to the Expression of Uncertainty in Measurement, Technical Report, JCGM, 2008.

[23] C. Gulenoglu, F. Akturk, S. Aradag, N. Sezer Uzol, S. Kakac, Experimental comparison of performances of three different plates for gasketed plate heat exchangers, Int. J. Therm. Sci. 75 (2014) 249–256, http://dx.doi.org/10.1016/j.ijthermalsci.2013.06.012.

[24] J. Huang, Performance Analysis of Plate Heat Exchangers Used as Refrigerant Evaporators (Ph.D. thesis), University of the Witwatersrand, 2010.

[25] F. Warnakulasuriya, W. Worek, Heat transfer and pressure drop properties of high viscous solutions in plate heat exchangers, Int. J. Heat Mass Transfer 51 (1) (2008) 52–67, http://dx.doi.org/10.1016/j.ijheatmasstransfer.2007.04.054.

[26] A. Muley, R.M. Manglik, H.M. Metwally, Enhanced heat transfer characteristics of viscous liquid flows in a chevron plate heat exchanger, J. Heat Transfer 121 (4) (1999) 1011–1017, http://dx.doi.org/10.1115/1.2826051.

[27] A. Muley, R.M. Manglik, Experimental study of turbulent flow heat transfer and pressure drop in a plate heat exchanger with chevron plates, J. Heat Transfer 121 (1) (1999) 110–117, http://dx.doi.org/10.1115/1.2825923.

[28] O. Arsenyeva, L. Tovazhnyansky, P. Kapustenko, G. Khavin, The generalized correlation for friction factor in criss-cross flow channels of plate heat exchangers, Chem. Eng. Trans. 25 (2011) 399–404, http://dx.doi.org/10.3303/CET1125067.

[29] H. Martin, A theoretical approach to predict the performance of chevron-type plate heat exchangers, Chem. Eng. Process. Process Intensif. 35 (4) (1996) 301–310, http://dx.doi.org/10.1016/0255-2701(95)04129-X.

[30] A.E. Dukler, M. Wicks, R.G. Cleveland, Frictional pressure drop in two-phase flow: B. An approach through similarity analysis, AIChE J. 10 (1964) 44–51.

[31] K. Nilpueng, S. Wongwises, Two-phase gas-liquid flow characteristics inside a plate heat exchanger, Exp. Therm Fluid Sci. 34 (2010) 1217–1229, http://dx.doi.org/10.1016/j.expthermflusci.2010.05.001.

[32] J. Hinze, Fundamentals of the hydrodynamic mechanism of splitting in dispersion processes, AIChE J. 1 (1955) 289–295, http://dx.doi.org/10.1002/aic.690010303.

[33] Y. Taitel, D. Barnea, A.E. Dukler, Modelling flow pattern transitions for steady upward gas-liquid flow in vertical tubes, AIChE J. 26 (1980) 345–354, http://dx.doi.org/10.1002/aic.690260304.